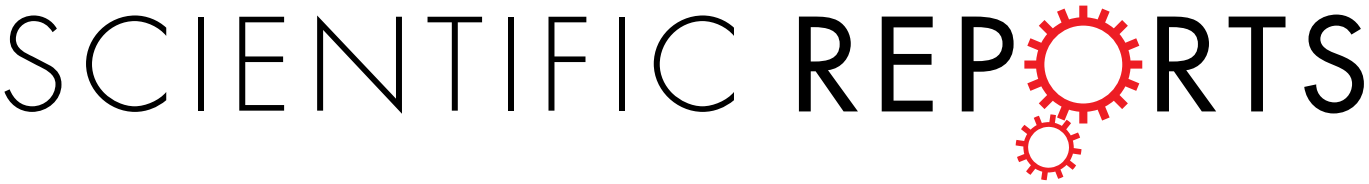

OPEN

Two-Dimensional $Mo_xW_{1-x}S_2$ Graded Alloys: Growth and Optical Properties

Received: 25 May 2018
Accepted: 14 August 2018
Published online: 27 August 2018

Kevin Bogaert[1,2], Song Liu[2], Tao Liu[2,3], Na Guo[2,3], Chun Zhang[2,3,4], Silvija Gradečak[1,5] & Slaven Garaj[2,3,6]

Two-dimensional (2D) transition metal dichalcogenides can be alloyed by substitution at the metal atom site with negligible effect on lattice strain, but with significant influence on optical and electrical properties. In this work, we establish the relationship between composition and optical properties of the $Mo_xW_{1-x}S_2$ alloy by investigating the effect of continuously-varying composition on photoluminescence intensity. We developed a new process for growth of two-dimensional $Mo_xW_{1-x}S_2$ alloys that span nearly the full composition range along a single crystal, thus avoiding any sample-related heterogeneities. The graded alloy crystals were grown using a diffusion-based chemical vapor deposition (CVD) method that starts by synthesizing a WS_2 crystal with a graded point defect distribution, followed by Mo alloying in the second stage. We show that point defects promote the diffusion and alloying, as confirmed by Raman and photoluminescence measurements, density functional theory calculations of the reaction path, and observation that no alloying occurs in CVD-treated exfoliated crystals with low defect density. We observe a significant dependence of the optical quantum yield as a function of the alloy composition reaching the maximum intensity for the equicompositional $Mo_{0.5}W_{0.5}S_2$ alloy. Furthermore, we map the growth-induced strain distribution within the alloyed crystals to decouple composition and strain effects on optical properties: at the same composition, we observe significant decrease in quantum yield with induced strain. Our approach is generally applicable to other 2D materials as well as the optimization of other composition-dependent properties within a single crystal.

Two-dimensional (2D) transition metal dichalcogenides (TMDs) are layered semiconducting materials with an array of interesting properties, including a direct bandgap[1,2], large exciton binding energy[3], large spin orbit coupling[4], and a high degree of band structure tunability via surface dopants[5–7] and alloying[8–26], which make them desirable for optical, electronic, and energy generation applications[27–33].

In analogy to conventional semiconductors, substituting various transition metal (M = Mo, W, etc.) and chalcogen (X = S, Se, Te) atoms into the TMD lattice while maintaining an MX_2 stoichiometry would enable property modulation for specific applications. Whereas spatially uniform TMD alloying offers a choice of material properties within a range given by its pure TMD components, graded TMD alloying – in which the composition gradually varies across the crystal – introduces anisotropic behavior in the bandgap, optical properties and spin-orbit coupling that could be implemented, for example, in future excitonic devices[34]. The previous studies of alloyed TMDs have demonstrated that the photoluminescence (PL) bandgap emission energy is tunable as a function of composition, but most of these studies used discrete crystals with a specific alloy composition. This approach hinders understanding of the intrinsic relationship between PL quantum yield and composition, as it does not account for non-compositional factors between different crystals (*e.g.*, substrate interactions, strain profile, defect

[1]Department of Materials Science and Engineering, Massachusetts Institute of Technology, 77 Massachusetts Avenue, Cambridge, MA, 02139, USA. [2]Centre for Advanced 2D Materials, National University of Singapore, 6 Science Drive 2, 117546, Singapore, Singapore. [3]Department of Physics, National University of Singapore, 2 Science Drive 3, 117542, Singapore, Singapore. [4]Department of Chemistry, National University of Singapore, 3 Science Drive 3, 117543, Singapore, Singapore. [5]Low Energy Electronic Systems Interdisciplinary Research Group, Singapore-MIT Alliance in Research and Technology, 1 CREATE Way, 138602, Singapore, Singapore. [6]Department of Biomedical Engineering, National University of Singapore, 9 Engineering Drive 1, 117575, Singapore, Singapore. Correspondence and requests for materials should be addressed to S. Garaj (email: slaven@nus.edu.sg)

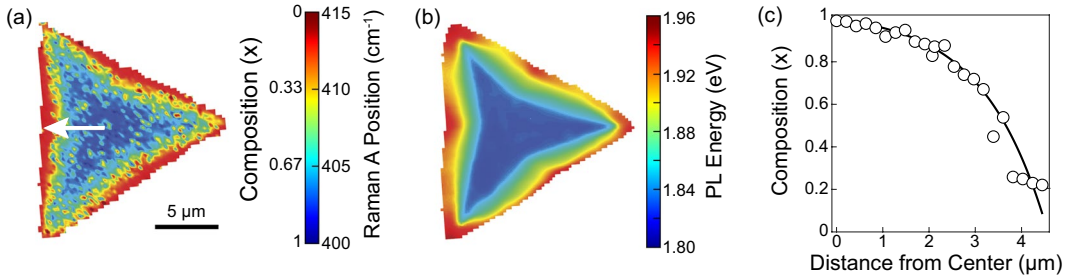

Figure 1. (**a**) Raman position of the A vibrational mode (and thus the composition x) of a $Mo_xW_{1-x}S_2$ graded alloy crystal. Scale bar is 5 μm. (**b**) Corresponding PL peak energy map. (**c**) Crystal composition as a function of the position along the arrow shown in (a) determined using the Raman A vibrational mode. The line is a guide for eye.

density, etc.) that could influence the optical properties (*e.g.*, charge transfer doping, band structure modification, creation of trap states, etc.).

To circumvent this limitation, we study optical properties of 2D TMDs with compositional variations within single crystals that were produced using a novel 2-step chemical vapor deposition (CVD) process based on diffusion-mediated growth method. In the first step, WS_2 crystals are grown via CVD, which are then exposed to MoS_2 precursors in the second step. The resulting crystals show unexpected compositional variations where Mo atoms diffuse and replace W atoms inside the crystals[17]. In this work – driven by a hypothesis that the alloying is facilitated by point defects – we introduce the graded distribution of point defects into the template WS_2 crystal by mixing the metal precursor (WO_3) with NaCl admixture that is known to reduce its vaporization temperature[35]. As a result, in the second CVD step, the diffusion of Mo results in a unique graded alloy structure mirroring the starting defect distribution. By having the ability to tune composition within a single crystal, we demonstrate composition-dependent variations in PL intensity that are intrinsic to the material, and not an artifact of the sample preparation. Moreover, we decouple strain- and composition-related optical properties assessing the role of substrate in future applications of 2D TMDs. Here we focus on $Mo_xW_{1-x}S_2$ alloys, but our synthesis method and the general approach is generally applicable across various TMD platforms.

Results and Discussion

Details of the synthesis are described in the Methods section. In short, to produce compositionally-graded $Mo_xW_{1-x}S_2$ 2D single crystals, WS_2 crystals were first grown at 825 °C using WO_3/NaCl precursor, followed by the deposition of MoS_2 at 680 °C. Figure 1a shows the Raman A vibrational mode of a representative resulting single crystal and the corresponding optical microscopy and atomic force microscopy (AFM) images are provided in the Supporting Information, Figure S1. It has been demonstrated that the position of the A vibrational mode shifts linearly over the composition range from ~403 cm^{-1} for pure MoS_2 ($x = 1$) to ~419 cm^{-1} for pure WS_2 ($x = 0$)[26]. As it can be seen in Fig. 1a, the A mode in our crystals changes gradually from 400 cm^{-1} in the center of the crystal to 415 cm^{-1} toward the crystal edges, thus demonstrating continuously changing $Mo_xW_{1-x}S_2$ composition. The PL peak energy map of the same crystal (Fig. 1b) corroborates the Raman results shown in Fig. 1a. The exciton emission energies of pure MoS_2 and WS_2 are 1.82 eV and 1.97 eV, respectively[36], whereas the measured PL energy range spans from 1.82 eV to 1.95 eV starting from the crystal core toward edges, respectively. An additional example of a crystal demonstrating this behavior is presented in Supporting Figure S2. Taken together, these results indicate that the crystal has a three-fold symmetry with pure MoS_2 in the core and gradually-shifted composition toward the crystal edges that are composed of almost pure WS_2. This gradient in composition is quantified in Fig. 1c, calculated from the Raman data presented in Fig. 1a.

This graded spatial variation of composition seen in the final alloyed crystal structure was enabled by engineering a spatially heterogeneous concentration of point defects in the starting WS_2 crystals. Figure S3 in Supporting Information shows a Raman spectrum and the Raman intensity ratio map that compares LA(M) and A vibrational modes of a template WS_2 crystal grown using the NaCl-based CVD method. It has been previously shown that the LA(M)/A Raman intensity ratio is proportional to the inverse square of the distance between point defects with low-defect crystals having a ratio of 0.10–0.15[37]. WS_2 crystals grown without NaCl show a uniform ratio $\leq$0.15;[17] in contrast, WS_2 crystals grown using NaCl are more defective with the ratio ranging from 1.05 at the crystal core to 0.80 at the edges. The graded LA(M)/A intensity ratio present in NaCl-assisted WS_2 crystals is indicative of a graded point defect distribution, with a greater density of defects near the crystal core compared to the exterior. This is likely due to a W-rich atmosphere during early stages of the crystal growth leading to non-stoichiometric crystal growth and formation of sulfur vacancies. This result indicates that the higher density of point defects in the core of the starting WS_2 crystal enhances Mo diffusion and results in the graded Mo concentration in the resulting alloyed structure.

To further probe the role of defects in our novel graded alloy synthesis method, we mechanically exfoliated WS_2 or MoS_2 template crystals – having a low defect density – and employed second stage CVD growth of the complementary material (Fig. 2). A WS_2 crystal was first exfoliated and deposited onto a substrate, followed by the standard MoS_2 CVD deposition. Figure 2a shows the A Raman vibrational mode for the resulting crystal. As evidenced by the sharp interface between the mechanically exfoliated WS_2 (A position ≈415 cm^{-1}) and CVD-grown MoS_2 (A position ≈405 cm^{-1}) regions, no alloying or diffusion has taken place. A comparable sharp

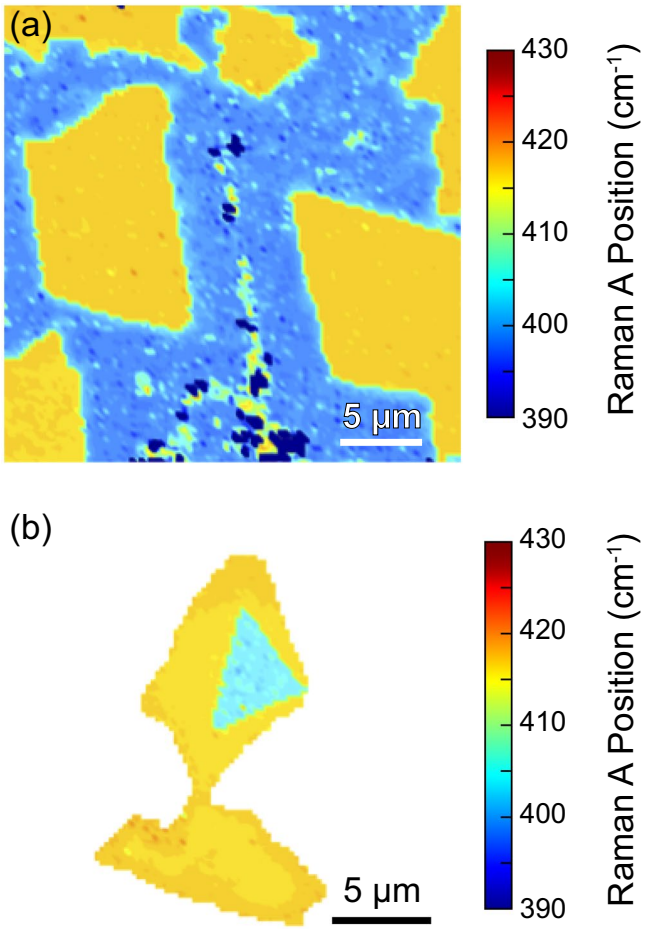

Figure 2. Raman position of the A vibrational mode for (**a**) exfoliated WS_2 (yellow) followed by CVD-grown MoS_2 (blue) and (**b**) exfoliated MoS_2 (blue) followed by CVD-grown WS_2 (yellow). Both growths result in a lateral heterostructure with a sharp interface and chronological core-shell configuration indicating that no significant amount of diffusion occurred. Scale bars are 5 μm.

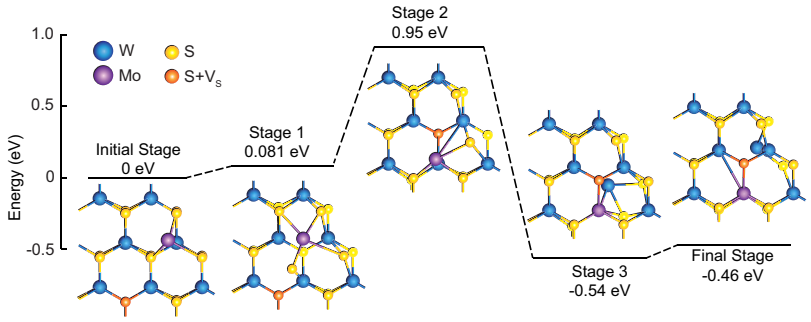

Figure 3. DFT-calculated proposed reaction path and schematics of atomic configurations for inward diffusion of a Mo atom and outward diffusion of a W atom and S vacancy. From the Initial Stage to Stage 2, a Mo adatom and S atom diffuse inward together, resulting in the outward diffusion of a S vacancy. From Stage 2 to the Final Stage, the Mo adatom incorporates into the metal plane of atoms, displacing a W atom, which then diffuses outward through the S vacancy site to the crystal edge. This reaction is exothermic.

interface is observed for crystals with the inverse configuration, consisting of a mechanically exfoliated MoS_2 core and the surrounding CVD-grown WS_2 (Fig. 2b).

To gain microscopic insight into the diffusion process, we performed density functional theory (DFT) modeling and explored possible diffusion-exchange mechanisms and energetics of the most likely exchange path for Mo and W atoms (Fig. 3). The DFT model consisted of a triangular single-layer WS_2 crystal with 45 W atoms and 103 S atoms, as shown in Figure S4 of the Supporting Information. A S vacancy, as the most probable point defect

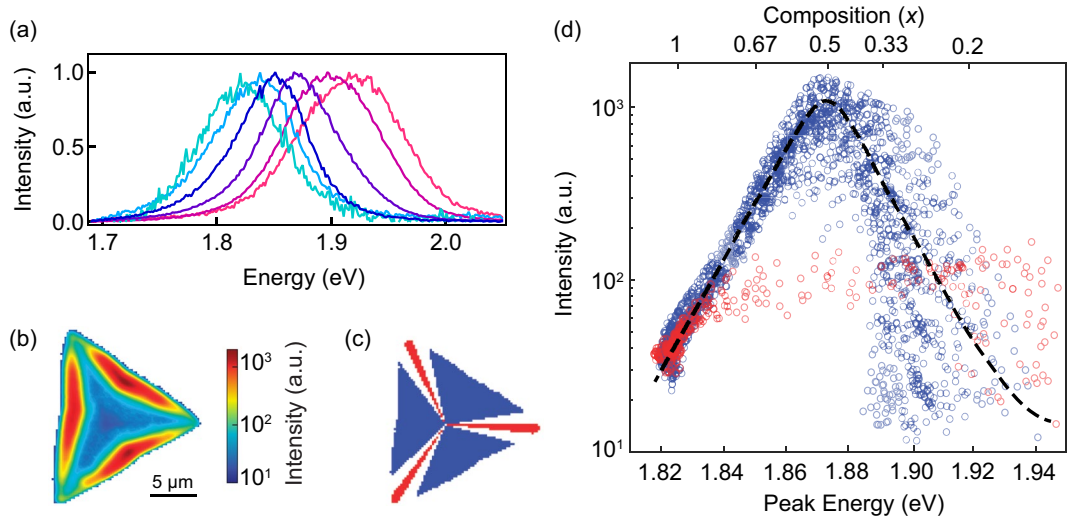

Figure 4. (**a**) Normalized PL spectral evolution from the crystal core (cyan, left-most spectrum) toward the edge (red, right-most spectrum). Spectra are individually fitted to double-Gaussian distributions and show a continuous change in peak emission energy corresponding to local alloy composition. (**b**) Spatial map of the photoluminescence (PL) intensity within the crystal shown in Fig. 1, plotted on a log scale. (**c**) Color-coded map of the crystal indicates PL data points extracted for the unstrained (blue) and strained (red) regions, as shown in (d). From the crystal center, all pixels of the crystal within 1.5 degrees of the symmetry lines connecting the center to the corners are colored red, indicating regions of greatest strain. All pixels greater than 6 degrees away from the symmetry lines are colored blue, indicating regions of least strain. (**d**) PL peak energy *vs*. intensity of the graded alloy crystal. Top scale shows the corresponding composition *x* determined from Raman measurements (we note that the scale is not linear due to non-linear relation between the PL peak energy and the composition). The blue(red) data points in the graph were taken from the blue(red) (*i.e*. unstrained(strained)) regions of panel (c). Dashed line is a guide for eye for the unstrained data, which mostly follows the average value of the blue data points.

in the crystal[38], was placed in the interior of the WS_2 lattice in the upper plane of chalcogen atoms. The adsorption of a single Mo impurity atom was then tested on all possible sites of the crystal. The most stable adsorption configuration consists of a Mo atom adsorbed on top of an edge W atom in the vicinity of the S vacancy, which displaces the W atom downward. This configuration is depicted as the initial stage in Fig. 3. In stage 1, the Mo atom and one neighboring S atom diffuse toward the S vacancy to temporarily form antisite defects until they eventually reach the vacancy in stage 2. At this point, the S atom fills in the original S vacancy – thereby creating a new vacancy site in the upper plane of chalcogen atoms – and the Mo atom is positioned on top of a different W atom within the crystal. In stage 3, the S atom moves from the lower plane of chalcogen atoms to the upper plane of chalcogen atoms and the Mo atom moves downward into the plane of metal atoms, forcing the W atom to occupy the S vacancy site in the lower plane of chalcogen atoms. In the final stage, the W atom is expelled further toward the crystal edge to the metal site. It is important to note that the system is capable of overcoming the stage 2 energy barrier at the experimentally tested growth temperatures. Altogether, this process demonstrates a thermodynamically viable mechanism for the inward diffusion of Mo atoms accompanied by an outward diffusion of W atoms and S vacancies, turning a relatively defective WS_2 crystal into a higher quality crystal with a Mo-rich core. This mechanism corroborates and helps to explain the S vacancy-Mo coupling in W-rich $Mo_xW_{1-x}S_2$ reported by Azizi *et al.*[39].

The unique graded structure allows us now to investigate the material properties as a function of the composition within a single crystal, thus obtained under identical synthesis conditions. Here we focus on developing understanding of the PL quantum yield as a function of the $Mo_xW_{1-x}X_2$ alloy composition. Figure 4a shows normalized position-dependent PL spectra that demonstrate a continuous transition from MoS_2-like emission near the crystal core to WS_2-like emission near the crystal edges. A good fit can be obtained for each emission spectrum, providing a reliable measurement of the PL peak intensity and energy. By comparing Raman and PL peak energy maps shown in Fig. 1a,b, respectively, we can determine correlation between the local crystal composition and corresponding PL energy, shown in Figure S5 of the Supporting Information.

Furthermore, composition-dependent PL intensity gives us an important insight into the relationship between PL quantum yield and the alloy composition. Although PL quantum yield specifically refers to the ratio between electron-hole pairs generated and photons radiated, we can make reasonably accurate relative comparisons from PL intensity fluctuations within a single measurement because the laser power density and acquisition time are constant, the absorbance for monolayer MoS_2 and WS_2 at 532 nm are approximately equal[40], and the effects of exciton funneling are assumed to be negligible. Figure 4b maps the intensity of the PL peak determined by fitting individual PL spectra as a function of the position. By plotting the PL intensity along the lines that connect the crystal core to the triangle sides (sketched blue in Fig. 4c), it can be observed that PL intensity increases and decreases exponentially as a function of the PL energy, with the maximum PL intensity centered at ~1.87 eV (Fig. 4d).

This result suggests that the maximum PL quantum yield in $Mo_xW_{1-x}X_2$ system occurs for an alloy (in our case, for $x \approx 0.5$) rather than for either of the pure extrema (MoS_2 or WS_2). In contrast to previous reports that have focused on either pure WS_2 and MoS_2[41] or limited-range, Mo-rich $Mo_xW_{1-x}Se_2$[42], our results probe the PL quantum yield for nearly the entire $Mo_xW_{1-x}S_2$ alloy spectrum.

Similar PL enhancement has been reported in ternary alloys of III–V semiconductors[43,44]. In those material systems, the enhanced radiative recombination has been attributed to reduced carrier mobility resulting in enhanced carrier localization. However, due to the large exciton binding energy of 2D TMDs[3], the analogy between the two systems is not straight-forward. Instead, the PL enhancement could be the result of a decrease in concentration of non-radiative point-defect related deep levels in the alloy, as theoretically predicted[45].

In addition, our results indicate that the PL quantum yield of $Mo_xW_{1-x}X_2$ materials is also sensitive to strain. Figure 4d shows that the PL intensity is reduced by more than an order of magnitude for the same PL energy/crystal composition when measured from the crystal core toward the corners (sketched red in Fig. 4c). Generally, the strain accumulates at the corners due to the significant difference in temperature between growth conditions (825 °C for WS_2 and 680 °C for MoS_2) and room temperature as well as the difference in the coefficient of thermal expansion between TMDs and the substrate, SiO_2[15,17,25,46–48]. In our crystals, this strain is evidenced in AFM height and phase maps (Supporting Figure S6). Given the low PL intensity in the strained regions at all compositions, we can conclude that the strain-dependent effects on PL quantum yield supersede the composition-dependent effects. Therefore, it is evident that strain must be well-controlled, whether through crystal transfer[49], substrate choice[50], or other means, to control the luminescence yield regardless of crystal composition.

In conclusion, we have established the relationship between PL intensity and alloy composition (x) within single crystals of $Mo_xW_{1-x}S_2$ graded alloys that span nearly the entire composition range. Our results show an exponential increase of the quantum yield with increased alloying, reaching the maximum value for equicompositional alloy $Mo_{0.5}W_{0.5}S_2$ ($x = 0.5$), which is two orders of magnitude enhanced compared to the values for pure MoS_2 ($x = 1$) and pure WS_2 ($x = 0$). Such observation is consistent with theoretical prediction that alloying could suppress the deep in-gap level responsible for non-radiative recombination, and offers the venue for improving optical performance of TMD materials. Additionally, we demonstrated that the introduction of the strain leads to suppression of PL intensity for all the compositions of the alloy. The synthesis of graded alloys was achieved by diffusion-driven metal exchange in the pure TMD template crystals. Our DFT calculations reveal a thermodynamically favorable diffusion-exchange reaction path for controlled alloying, controlled by the sulfur vacancies. Our approach can be extended to other TMDs and future experiments to engineer the defect distribution by other means (e.g. laser, O_2 plasma, annealing in air etc.) that would enable a higher degree of control over compositional tuning and patterning in a crystal. On-demand alloys such as these could be useful in several applications that require controlled, directional anisotropy of optical and/or electrical properties.

Methods

Sample Preparation. $Mo_xW_{1-x}S_2$ alloys were grown in two subsequent CVD steps at ambient pressure using Ar as a carrier gas. A bare Si wafer substrate with a 300-nm thick SiO_2 layer was suspended above an alumina boat containing the metal precursor powder at the center of the CVD furnace. Sulfur powder (Sigma-Aldrich, 99.5%), the chalcogen precursor, was placed in another alumina boat and was initially outside of the furnace, at the upstream end of the 1-inch quartz tube. Once the furnace reached the growth temperature, the sulfur was introduced to the upstream of the furnace using magnets to reach approximately 200 °C. In the first growth step, WS_2 crystals were grown at 825 °C for 30 min using tungsten trioxide (WO_3, Sigma-Aldrich, 99.9%) mixed with sodium chloride (NaCl) in a 9:2 mass ratio as the metal precursor with an Ar flow rate of 50 sccm. In the second growth step, the metal precursor was replaced with molybdenum trioxide (MoO_3, Sigma-Aldrich, 99.5%), the growth temperature was reduced to 680 °C and Ar flow rate to 25 sccm.

Exfoliated crystals were produced from bulk samples by mechanical exfoliation.

Sample Characterization. Optical images were recorded using a Leica DFC 450 C microscope. AFM images were recorded with a Bruker Dimension Fastscan AFM using a tapping mode. Raman and PL measurements were performed on WITec Alpha 300 R and Horiba Jobin Yvon LabRAM HR800 confocal Raman microscopes under ambient conditions at room temperature. A 532 nm laser was focused onto the sample using a 100× objective resulting in a spot size of ~1 μm in diameter. 1800 and 600 lines/mm grating were used in Raman and PL measurements, respectively.

DFT Calculations. Computational results utilize density functional theory implemented in Vienna ab-initio Simulation Package[51,52]. The plane-wave basis with the cut-off energy of 400 eV and the generalized gradient approximation in the Perdew-Burke-Ernzerhof (PBE) format[53] with the projector-augmented wave method[54] were employed in all calculations. The structural relaxations were carried out until the Hellmann-Feynman force on each atom is less than 0.01 eV/Å, and the energy convergence criterion was set to 10^{-5} eV. Gamma-point-only k sampling is adopted for calculations.

References

1. Splendiani, A. *et al*. Emerging photoluminescence in monolayer MoS_2. *Nano Lett.* **10**, 1271–1275 (2010).
2. Mak, K. F., Lee, C., Hone, J., Shan, J. & Heinz, T. F. Atomically thin MoS_2: A new direct-gap semiconductor. *Phys. Rev. Lett.* **105**, 136805 (2010).
3. Cheiwchanchamnangij, T. & Lambrecht, W. R. L. Quasiparticle band structure calculation of monolayer, bilayer, and bulk MoS_2. *Phys. Rev. B* **85**, 205302 (2012).
4. Zhu, Z. Y., Cheng, Y. C. & Schwingenschlögl, U. Giant spin-orbit-induced spin splitting in two-dimensional transition-metal dichalcogenide semiconductors. *Phys. Rev. B* **84**, 153402 (2011).
5. Nguyen, E. P. *et al*. Electronic tuning of 2D MoS_2 through surface functionalization. *Adv. Mater.* **27**, 6225–6229 (2015).
6. Pierucci, D. *et al*. Tunable doping in hydrogenated single layered molybdenum disulfide. *ACS Nano* **11**, 1755–1761 (2017).

7. Kang, M. *et al*. Universal mechanism of band-gap engineering in transition-metal dichalcogenides. *Nano Lett.* **17**, 1610–1615 (2017).
8. Chen, Y. *et al*. Tunable band gap photoluminescence from atomically thin transition-metal dichalcogenide alloys. *ACS Nano* **7**, 4610–4616 (2013).
9. Mann, J. *et al*. 2-Dimensional transition metal dichalcogenides with tunable direct band gaps: $MoS_{2(1-x)}Se_{2x}$ monolayers. *Adv. Mater.* **26**, 1399–1404 (2014).
10. Lin, Z. *et al*. Facile synthesis of MoS_2 and $Mo_xW_{1-x}S_2$ triangular monolayers. *APL Mater.* **2**, 092514 (2014).
11. Liu, H., Antwi, K. K. A., Chua, S. & Chi, D. Vapor-phase growth and characterization of $Mo_{1-x}W_xS_2$ ($0 \leq x \leq 1$) atomic layers on 2-inch sapphire substrates. *Nanoscale* **6**, 624–629 (2014).
12. Feng, Q. *et al*. Growth of large-area 2D $MoS_{2(1-x)}Se_{2x}$ semiconductor alloys. *Adv. Mater.* **26**, 2648–2653 (2014).
13. Li, H. *et al*. Lateral growth of composition graded atomic layer $MoS_{2(1-x)}Se_{2x}$ nanosheets. *J. Am. Chem. Soc.* **137**, 5284–5287 (2015).
14. Zheng, S. *et al*. Monolayers of $W_xMo_{1-x}S_2$ alloy heterostructure with in-plane composition variations. *Appl. Phys. Lett.* **106**, 063113 (2015).
15. Kobayashi, Y., Mori, S., Maniwa, Y. & Miyata, Y. Bandgap-tunable lateral and vertical heterostructures based on monolayer $Mo_{1-x}W_xS_2$ alloys. *Nano Res.* **8**, 3261–3271 (2015).
16. Fu, Q. *et al*. Synthesis and enhanced electrochemical catalytic performance of monolayer $WS_{2(1-x)}Se_{2x}$ with a tunable band gap. *Adv. Mater.* **27**, 4732–4738 (2015).
17. Bogaert, K. *et al*. Diffusion-mediated synthesis of MoS_2/WS_2 lateral heterostructures. *Nano Lett.* **16**, 5129–5134 (2016).
18. Huang, J. *et al*. Stable electrical performance observed in large-scale monolayer $WSe_{2(1-x)}S_{2x}$ with tunable band gap. *Nanotechnology* **27**, 13LT01 (2016).
19. Azizi, A. *et al*. Spontaneous formation of atomically thin stripes in transition metal dichalcogenide monolayers. *Nano Lett.* **16**, 6982–6987 (2016).
20. Rhodes, D. *et al*. Engineering the structural and electronic phases of $MoTe_2$ through W substitution. *Nano Lett.* **17**, 1616–1622 (2016).
21. Li, H. *et al*. Composition-modulated two-dimensional semiconductor lateral heterostructures via layer-selected atomic substitution. *ACS Nano* **11**, 961–967 (2017).
22. Wu, X. *et al*. Spatially composition-modulated two-dimensional $WS_{2x}Se_{2(1-x)}$ nanosheets. *Nanoscale* **9**, 4707–4712 (2017).
23. Chen, F., Wang, L., Ji, X. & Zhang, Q. Temperature-dependent two-dimensional transition metal dichalcogenide heterostructures: controlled synthesis and their properties. *ACS Appl. Mater. Interfaces* **9**, 30821–30831 (2017).
24. Ullah, F. *et al*. Growth and simultaneous valleys manipulation of two-dimensional $MoSe_2$-WSe_2 lateral heterostructure. *ACS Nano* **11**, 8822–8829 (2017).
25. Wang, Z. Q. *et al*. Chemical vapor deposition of monolayer $Mo_{1-x}W_xS_2$ crystals with tunable band gaps. *Sci. Rep* **6**, 21536 (2016).
26. Chen, Y. *et al*. Composition-dependent Raman modes of $Mo_{1-x}W_xS_2$ monolayer alloys. *Nanoscale* **6**, 2833–2839 (2014).
27. Withers, F. *et al*. Light-emitting diodes by band-structure engineering in van der Waals heterostructures. *Nat. Mater.* **14**, 301–306 (2015).
28. Jariwala, D., Sangwan, V. K., Lauhon, L. J., Marks, T. J. & Hersam, M. C. Emerging device applications for semiconducting two-dimensional transition metal dichalcogenides. *ACS Nano* **8**, 1102–1120 (2014).
29. Pospischil, A., Furchi, M. M. & Mueller, T. Solar-energy conversion and light emission in an atomic monolayer p-n diode. *Nat. Nanotechnol.* **9**, 257–261 (2014).
30. Ross, J. S. *et al*. Electrically tunable excitonic light-emitting diodes based on monolayer WSe_2 p-n junctions. *Nat. Nanotechnol.* **9**, 268–272 (2014).
31. Radisavljevic, B., Radenovic, A., Brivio, J., Giacometti, V. & Kis, A. Single-layer MoS_2 transistors. *Nat. Nanotechnol.* **6**, 147–150 (2011).
32. Chhowalla, M. *et al*. The chemistry of two-dimensional layered transition metal dichalcogenide nanosheets. *Nat. Chem.* **5**, 263–275 (2013).
33. Lin, Z. *et al*. 2D materials advances: from large scale synthesis and controlled heterostructures to improved characterization techniques, defects and applications. *2D Mater.* **3**, 042001 (2016).
34. Onga, M., Zhang, Y., Ideue, T. & Iwasa, Y. Exciton Hall effect in monolayer MoS_2. *Nat. Mater.* **216**, 1193–1197 (2017).
35. Li, S. *et al*. Halide-assisted atmospheric pressure growth of large WSe_2 and WS_2 monolayer crystals. *Appl. Mater. Today* **1**, 60–66 (2015).
36. Gong, Y. *et al*. Vertical and in-plane heterostructures from WS_2/MoS_2 monolayers. *Nat. Mater.* **13**, 1135–1142 (2014).
37. McCreary, A. *et al*. Distinct photoluminescence and Raman spectroscopy signatures for identifying highly crystalline WS_2 monolayers produced by different growth methods. *J. Mater. Res.* **31**, 931–944 (2016).
38. Zhou, W. *et al*. Intrinsic structural defects in monolayer molybdenum disulfide. *Nano Lett.* **13**, 2615–2622 (2013).
39. Azizi, A. *et al*. Defect coupling and sub-angstrom structural distortions in $W_{1-x}Mo_xS_2$ monolayers. *Nano Lett.* **17**, 2802–2808 (2017).
40. Li, Y. *et al*. Measurement of the optical dielectric function of monolayer transition-metal dichalcogenides: MoS_2, $MoSe_2$, WS_2, and WSe_2. *Phys. Rev. B* **90**, 205422 (2014).
41. Amani, M. *et al*. Recombination kinetics and effects of superacid treatment in sulfur- and selenium-based transition metal dichalcogenides. *Nano Lett.* **16**, 2786–2791 (2016).
42. Li, X. *et al*. Suppression of defects and deep levels using isoelectronic tungsten substitution in monolayer $MoSe_2$. *Adv. Funct. Mater.* **27**, 1603850 (2016).
43. Schubert, E. F., Göbel, E. O., Horikoshi, Y., Ploog, K. & Queisser, H. J. Alloy broadening in photoluminescence spectra of $Al_xGa_{1-x}As$. *Phys. Rev. B* **30**, 813–820 (1984).
44. Collins, C. J. *et al*. Enhanced room-temperature luminescence efficiency through carrier localization in $Al_xGa_{1-x}N$ alloys. *Appl. Phys. Lett.* **86**, 031916 (2005).
45. Huang, B., Yoon, M., Sumpter, B. G., Wei, S.-H. & Liu, F. Alloy engineering of defect properties in semiconductors: Suppression of deep levels in transition-metal dichalcogenides. *Phys. Rev. Lett.* **115**, 126806 (2015).
46. Alharbi, A. & Shahrjerdi, D. Electronic properties of monolayer tungsten disulfide grown by chemical vapor deposition. *Appl. Phys. Lett.* **109**, 193502 (2016).
47. McCreary, K. M. *et al*. The effect of preparation conditions on Raman and photoluminescence of monolayer WS_2. *Sci. Rep.* **6**, 35154 (2016).
48. Meng, L. *et al*. Two dimensional WS_2 lateral heterojunctions by strain modulation. *Appl. Phys. Lett.* **108**, 263104 (2016).
49. Amani, M. *et al*. High luminescence efficiency in MoS_2 grown by chemical vapor deposition. *ACS Nano* **10**, 6535–6541 (2016).
50. Ahn, G. H. *et al*. Strain-engineered growth of two-dimensional materials. *Nat. Commun.* **8**, 608 (2017).
51. Kresse, G. & Hafner, J. Ab initio molecular dynamics for liquid metals. *Phys. Rev. B* **47**, 558 (1993).
52. Kresse, G. & Furthmu, J. Efficient iterative schemes for ab initio total-energy calculations using a plane-wave basis set. *Phys. Rev. B* **54**, 16 (1996).
53. Perdew, J. P. *et al*. Atoms, molecules, solids, and surfaces: Applications of the generalized gradient approximation for exchange and correlation. *Phys. Rev. B* **46**, 11 (1992).
54. Blöchl, P. E. Projector augmented-wave method. *Phys. Rev. B* **50**, 24 (1994).

Acknowledgements

This work was supported by the National Research Foundation, Prime Minister's Office, Singapore, through Competitive Research Program (Award No. NRF-CRP13-2014-03), the Singapore-MIT Alliance for Research and Technology's (SMART) Low Energy Electronic Systems (LEES) IRG and by the NRF Fellowship Program (Award No. NRF-NRFF2012-09).

Author Contributions

K.B., S.L. and T.L. performed the experiments. N.G. and C.Z. performed the density functional theory calculations. K.B. analyzed the data. K.B., S.G. and S.G. wrote the manuscript. All authors have read and discussed the manuscript.

Additional Information

Supplementary information accompanies this paper at https://doi.org/10.1038/s41598-018-31220-z.

Competing Interests: The authors declare no competing interests.

Publisher's note: Springer Nature remains neutral with regard to jurisdictional claims in published maps and institutional affiliations.